nature biotechnology

LETTERS

https://doi.org/10.1038/s41587-019-0033-2

Proliferation tracing with single-cell mass cytometry optimizes generation of stem cell memory-like T cells

Zinaida Good[1,2,3,4,5], Luciene Borges[4,9], Nora Vivanco Gonzalez[1,4,9], Bita Sahaf[6], Nikolay Samusik[2,3], Robert Tibshirani[7,8], Garry P. Nolan[2,3,5,10] and Sean C. Bendall[4,5,10]*

Selective differentiation of naive T cells into multipotent T cells is of great interest clinically for the generation of cell-based cancer immunotherapies. Cellular differentiation depends crucially on division state and time. Here we adapt a dye dilution assay for tracking cell proliferative history through mass cytometry and uncouple division, time and regulatory protein expression in single naive human T cells during their activation and expansion in a complex ex vivo milieu. Using 23 markers, we defined groups of proteins controlled predominantly by division state or time and found that undivided cells account for the majority of phenotypic diversity. We next built a map of cell state changes during naive T-cell expansion. By examining cell signaling on this map, we rationally selected ibrutinib, a BTK and ITK inhibitor, and administered it before T cell activation to direct differentiation toward a T stem cell memory (T_{SCM})-like phenotype. This method for tracing cell fate across division states and time can be broadly applied for directing cellular differentiation.

Cellular differentiation is a continuous and coordinated process that integrates cell-intrinsic and extrinsic signals, leading to changes in phenotype, proliferation and death. The linkage of cell division with time during differentiation, especially in human cell systems, remains elusive. Multiple cellular processes have been implicated in T-cell fate selection during an immune response, including asymmetric distribution of polarity proteins during initial division[1] and the varying cell-autonomous capabilities of individual antigen-specific T cells[2,3], but the relative contributions of these two processes to T-cell fate selection are not well defined[4]. Moreover, comparison of time-dependent and division-state-dependent changes to our knowledge has not yet been performed in any cell context. An improved model of early T-cell fate choices across time and divisions will help clarify the mechanistic underpinnings and serve as a guide in T-cell engineering efforts for clinical applications.

Mapping differentiation across time and division states in complex cellular systems requires simultaneous high-throughput measurements of phenotype, function and proliferative history in single cells across multiple time points. Despite advances in sequencing-based techniques for lineage tracing[5], a compatible method for measuring proliferative history is unavailable, and spectral overlap in flow-cytometry-based methods[6] precludes high-dimensional cell phenotyping across divisions. Cytometry by time of flight (CyTOF; mass cytometry)[7] is a powerful technique for high-throughput proteomic monitoring of single-cell phenotypes, but cannot yet track proliferative history. Starting with a fluorescent dye dilution approach[8,9], we have created a mass cytometry assay whereby the proliferative history of single cells across 0–7 divisions can be traced in complex cell mixtures while performing highly multiplexed single-cell analyses for function and phenotype.

This approach enabled understanding of primary T-cell differentiation in the context of T-cell expansion for cancer immunotherapy[10] and computationally uncouples time in culture from cell division state. By examining cell signaling on a map of cell state transitions, we selected treatment with the small molecule ibrutinib before expansion to skew early naive T-cell differentiation toward a subset resembling clinically desirable T stem cell memory (T_{SCM}) cells[11,12].

Fluorescent dye dilution assays[6], originally developed for T cells[8], are useful for counting cell divisions by flow cytometry. To adapt a carboxyfluorescein succinimidyl ester (CFSE) dilution assay[8,9] to mass cytometry, we exploited the structural similarity between CFSE and fluorescein isothiocyanate (FITC) to track changes in CFSE signal via a metal-labeled anti-FITC antibody (Fig. 1a). Dividing cells pass ~50% of CFSE to each daughter cell, providing a proxy for counting cell divisions.

With optimal CFSE detection conditions for mass cytometry (Supplementary Data 1), we confirmed nontoxic, homogeneous labeling of primary human $CD8^+$ T cells with 80 μM CFSE in the presence of serum[6] (data not shown). In contrast to anti-FITC monoclonal antibodies, a polyclonal antibody produced a strong and specific signal (Fig. 1b and Supplementary Figs. 1a–e). Flow cytometry and mass cytometry yielded an equivalent CFSE signal (Fig. 1c), with minimal background for mass cytometry, as is typical[7]. Lack of autofluorescence enabled us to detect an equivalent CFSE signal in other cell types, such as monocytes and dendritic cells (Supplementary Fig. 1f).

To test this method in resolving division states, we followed T-cell proliferation during ex vivo expansion for cancer immunotherapy[13]. We selected the rapid expansion protocol (REP)[10] as a model system (Fig. 1d) and could distinguish the CFSE-traced T cells from unlabeled accessory cells and discern ≥5 cell divisions using both flow and mass cytometry (Fig. 1e). Using mathematical

[1]PhD Program in Immunology, Stanford University, Stanford, CA, USA. [2]Baxter Laboratory in Stem Cell Biology, Stanford University, Stanford, CA, USA. [3]Department of Microbiology and Immunology, Stanford University, Stanford, CA, USA. [4]Department of Pathology, Stanford University, Stanford, CA, USA. [5]Parker Institute for Cancer Immunotherapy, San Francisco, CA, USA. [6]Cancer Institute, Department of Medicine, Stanford University, Stanford, CA, USA. [7]Department of Statistics, Stanford University, Stanford, CA, USA. [8]Department of Health Research and Policy, Stanford University, Stanford, CA, USA. [9]These authors contributed equally: Luciene Borges, Nora Vivanco Gonzalez. [10]These authors jointly directed this work: Garry P. Nolan, Sean C. Bendall. *e-mail: bendall@stanford.edu

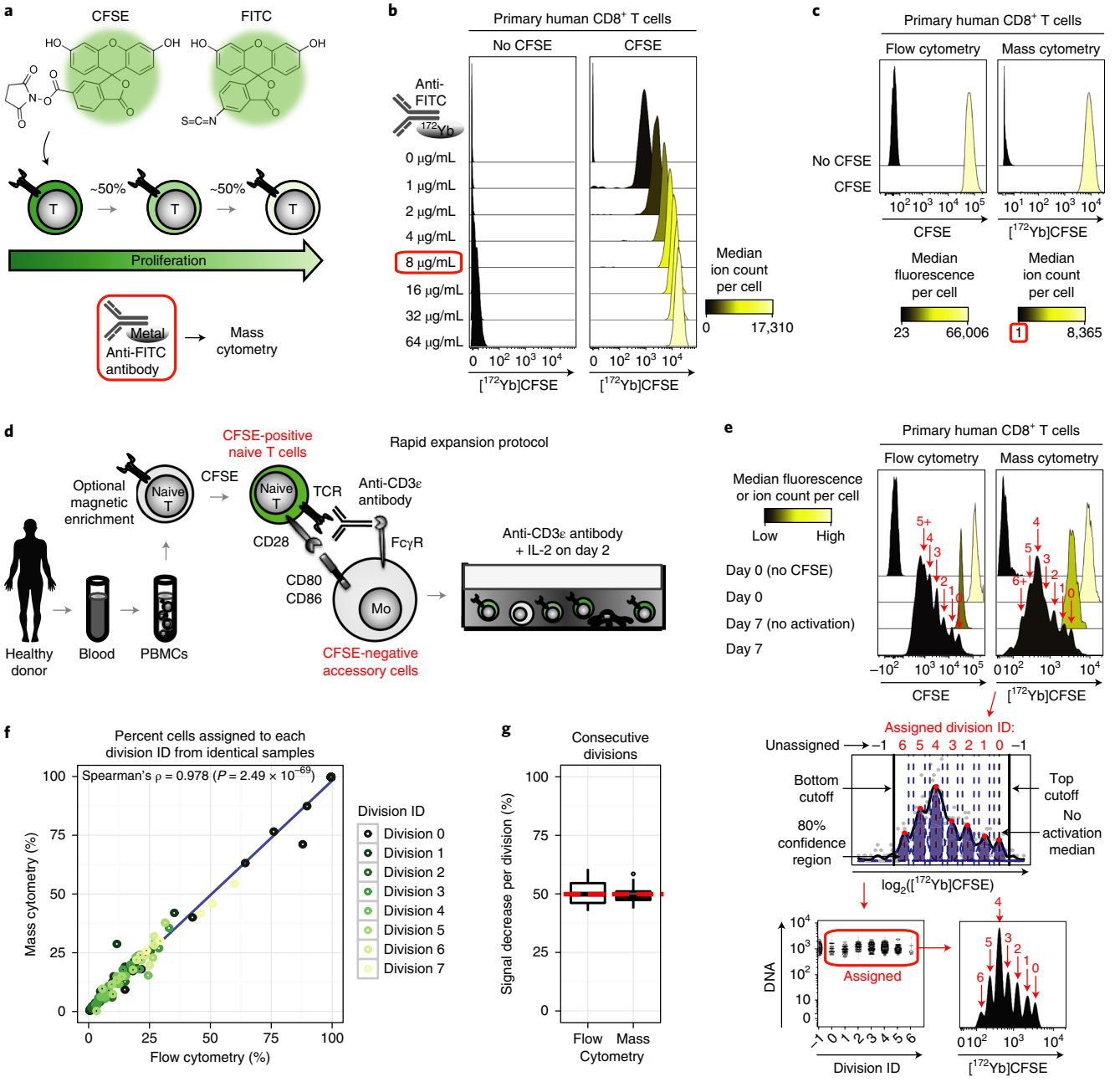

Fig. 1 | CFSE can be used to obtain proliferative history and trace cells of interest in complex cultures by mass cytometry. a, A strategy for adapting CFSE dye dilution assay to mass cytometry. Since both CFSE and FITC are derivatives of fluorescein, CFSE can be quantified by mass cytometry using intracellular staining with an anti-FITC antibody conjugated to a reporter metal isotope. With each division, daughter cells inherit ~50% of the CFSE, providing a proxy for estimating the number of cell divisions (proliferative history). **b**, Mass cytometry titration of polyclonal [^{172}Yb]anti-FITC on human CD8$^+$ T cells, with the optimal concentration highlighted (red box). **c**, Equivalent CFSE signal obtained from human CD8$^+$ T cells analyzed in parallel by flow cytometry and mass cytometry, with the near-zero [^{172}Yb]anti-FITC background highlighted (red box). **d**, Experimental outline for tracing proliferative history of naive CD8$^+$ T cells in REP as a model system. CFSE-labeled naive human T lymphocytes are induced to proliferate by CFSE-negative accessory cells, including monocytes (Mo), that present an anti-CD3ε antibody via Fcγ receptors (FcγRs) and express co-stimulatory molecules. IL-2 is added after 48 h. **e**, Proliferative history of CD8$^+$ T cells was similar whether measured directly by flow cytometry or indirectly using [^{172}Yb]anti-FITC by mass cytometry. A division ID (red arrows) was assigned to each cell falling into the ≥80% confidence region (blue); a division ID of -1 was assigned otherwise. Division IDs were added to the original file, enabling downstream analysis in software of choice, such as Cytobank. **f**, Spearman correlation analysis comparing percentage of cells falling into each division state in samples analyzed in parallel by flow cytometry and mass cytometry ($n = 26$ time-series samples from 6 REP cultures). **g**, CFSE signal reduction per division was calculated by geometric means from cells in **f**. Box plots show quartiles with a band at median, whiskers indicating 1.5 interquartile range (IQR), and outliers shown separately. A red dashed line indicates the expected 50% reduction. The antibody was titrated once; results in **c**,**e**–**g** are from 1 experiment representative of 3 experiments. Results in **b**,**c** and in **e**–**g** were obtained using the antibody panels in Supplementary Data 1 and Supplementary Data 2, respectively.

modeling based on local regression, we assigned division identifiers (IDs) to all cells falling into the ≥80% confidence region. The percentage of cells assigned to each division was nearly identical for samples analyzed by flow and mass cytometry (Spearman's rank correlation coefficient 0.978; Fig. 1f). Correlation in CFSE signal was also high for these samples (Spearman's rank correlation coefficient 0.997; Supplementary Fig. 2a). To estimate loss of signal without division, we applied linear regression to cells falling into the same division category over multiple days. If drifts were the same for flow and mass cytometry, we would expect the slope to be 1. We observed that this slope was consistently lower than 1 over division IDs 0–7 (mean ± s.d. = 0.496 ± 0.161; Supplementary Fig. 2b), suggesting that CFSE fluorescence is less stable than the CFSE epitopes detected in mass cytometry. As expected, CFSE signal decreased ~50% each time cells divided, and this was true irrespective of the cytometry method used (Fig. 2d) or time point assessed (Supplementary Fig. 2c).

With a panel of T-cell receptors relevant to immunotherapy and T-cell fate specification[11,12] (Supplementary Data 2–6), we reconciled early steps in naive CD8$^+$ T-cell differentiation with proliferation in REP. Although expression of a few proteins across divisions has previously been analyzed by flow cytometry[14], a high-dimensional analysis has not been performed. We tracked division state- and time-dependent dynamics of 23 markers after using 13 parameters for stringent selection of CFSE$^+$ CD8$^+$ T cells (DNA, size, viability, apoptotic status and lineage; Supplementary Fig. 3 and Supplementary Data 2) and additional parameters for data quality (normalization, barcoding). Tracking expression of individual proteins in CD8$^+$ T cells from the naive resting state showed that expression of some markers changed markedly as cells divided (Supplementary Fig. 4). For example, CD69^{low} T cells, which may be mistaken for poorly activated, had in fact divided the most, whereas regulatory protein expression (e.g., LAG3 and BTLA) remained consistent across divisions.

To computationally disentangle division-state-dependent from time-dependent changes, we normalized average marker expression to either division 0 for each day or the earliest time point for each division (Fig. 2a). Here, division-state-dependent changes, especially upregulation, were more pronounced than time-dependent changes in early T-cell differentiation during ex vivo expansion (Fig. 2b). Moreover, time-dependent changes were distinct from division-state-dependent changes. For example, expression of the activation molecule CD69 decreased with division at each time point yet changed little within each division over time. A multivariate regression model quantified the relative effects of division and time on levels of each regulatory protein (Fig. 2c). The strongest division-state-dependent effect was the switch from the CD45RA to CD45RO isoform, an important event in T-cell memory specification. In contrast, reduced phosphorylation of ribosomal protein S6 (pRPS6), downstream of mTOR, was predominantly time-dependent. Besides the expected connection between differentiation and time, the consistency and magnitude of division-state-dependent changes indicate a fundamental link between proliferation and differentiation of naive CD8$^+$ T cells in this expansion setting.

Notably, analysis of division state- and time-dependent changes revealed that phenotypic diversity, estimated by s.d. in individual protein expression, decreased consistently in a division- but not time-dependent manner for the majority of molecules examined (Supplementary Fig. 5). This, together with the link between differentiation and proliferation, prompted us to exploit the high-dimensional single-cell data to broadly map naive CD8$^+$ T-cell differentiation across division states.

To visualize high-dimensional single-cell data, we built force-directed graphs[15] using Vortex software[16]. The resulting maps aid the visualization of continuous processes, such as cellular differentiation[15]. Here, edges hold cells together with constant spring-like forces while forces proportional to cell dissimilarity in multidimensional protein expression mediate repulsion[15,16]. These repulsive and attractive forces eventually converge to a balanced state in which similar cells are located near each other and dissimilar cells are far apart. (This is not always the case in *t*-distributed stochastic neighbor embedding plots.) We modified Vortex to only allow edge connections either between consecutive time points, as in the FLOW-MAP algorithm[17], or between subsequent divisions to take advantage of our proliferative history data. This feature is now publicly available in Vortex. The single-cell phenotypic maps presented here connect cells only within neighboring division states (–1, 0, + 1).

We initially focused on day 3, when the majority of cells were in divisions 0 or 1 (Fig. 3a). At this early time in naive CD8$^+$ T-cell differentiation, undivided cells unexpectedly occupied the majority of phenotypic niches (dark green nodes, Fig. 3b). Partial cell activation is unlikely to contribute to this undivided cell diversity, since 99.2% of undivided cells in this culture were CD69^{high} (Supplementary Fig. 4b). We annotated this phenotypic map on the basis of all single-cell markers quantified (Supplementary Fig. 6). To understand how cells advance through phenotypic space, we applied diffusion maps[18]. This approach identifies the most likely sequence of cell state transitions, a metric called diffusion pseudo-time (DPT; Supplementary Fig. 7). Overlaying DPT onto our map exposed a continuum of phenotypes from the least differentiated to the two most differentiated states (Fig. 3c), which overlapped with three prominent regions in Fig. 3b. Importantly, undivided cells had the highest DPT diversity (estimated by s.d.) and completely covered the range of DPT values (Fig. 3d). Using lasso[19], we found that CD25 and CD137 had the highest coefficients predicting DPT1 and DPT2, respectively (Supplementary Data 7). This finding was corroborated by a correlation analysis (Supplementary Data 7).

As an independent metric of high-dimensional cellular diversity, we calculated angular distance to an average cell within each division (Fig. 3e). This metric confirmed that undivided cells had the highest phenotypic diversity, and phenotypic diversity significantly decreased with successive divisions (Fig. 3f). This observation held true on subsequent days (Fig. 3g and Supplementary Fig. 8).

To obtain an orthogonal view of diversity during early differentiation of naive CD8$^+$ T cells without a priori target bias, we performed droplet-based single-cell RNA-sequencing (RNA-seq) on CD8$^+$ T cells prospectively isolated from divisions 0, 1 or 2 on day 3 of REP (Fig. 3h and Supplementary Fig. 9). We then selected the 1,000 most variably expressed genes to construct a force-directed graph, which provides insight into biological identity of genes underlying cellular diversity (Fig. 3i and Supplementary Figs. 9–11). Undivided cells again occupied the majority of phenotypic niches and had a significantly higher phenotypic diversity than cells that divided either once or twice (Fig. 3j and Supplementary Fig. 12). Together, these data confirm that undivided CD8$^+$ T cells display the largest phenotypic diversity in our system.

By day 7 of differentiation, naive CD8$^+$ T cells expanded into new phenotypic niches and converged onto two main subpopulations (Fig. 4a,b and Supplementary Figs. 13–15), which resembled T_{SCM} and dysfunctional cells. T_{SCM} are minimally differentiated antigen-experienced T cells that are clinically favorable for immunotherapy because they show excellent engraftment, persistence and multifunctionality[11,12]. Clinically undesirable dysfunctional T cells express two or more inhibitory receptors and have poor proliferative capacity and effector functions[11]. Here, we define T_{SCM}-like cells as antigen-experienced (divided following T-cell antigen receptor (TCR) engagement) CD45RA^{high} CD45RO^{low} CD27^{high} CD127^{high} CCR7^{high} CTLA4^{low} LAG3^{low} PD1^{low} CD57^{low}, and dysfunctional-phenotype cells as antigen-experienced CD27^{low} CTLA4^{high} LAG3^{high} PD1^{high} (refs. [11,12,20]). Relative to T_{SCM}-like cells, dysfunctional-phenotype cells were CD45RA^{low} CD45RO^{high} CD5^{low} CD7^{low} CD25^{high} CD27^{low} CD52^{low} CD69^{high} CCR7^{low} and contained a subpopulation

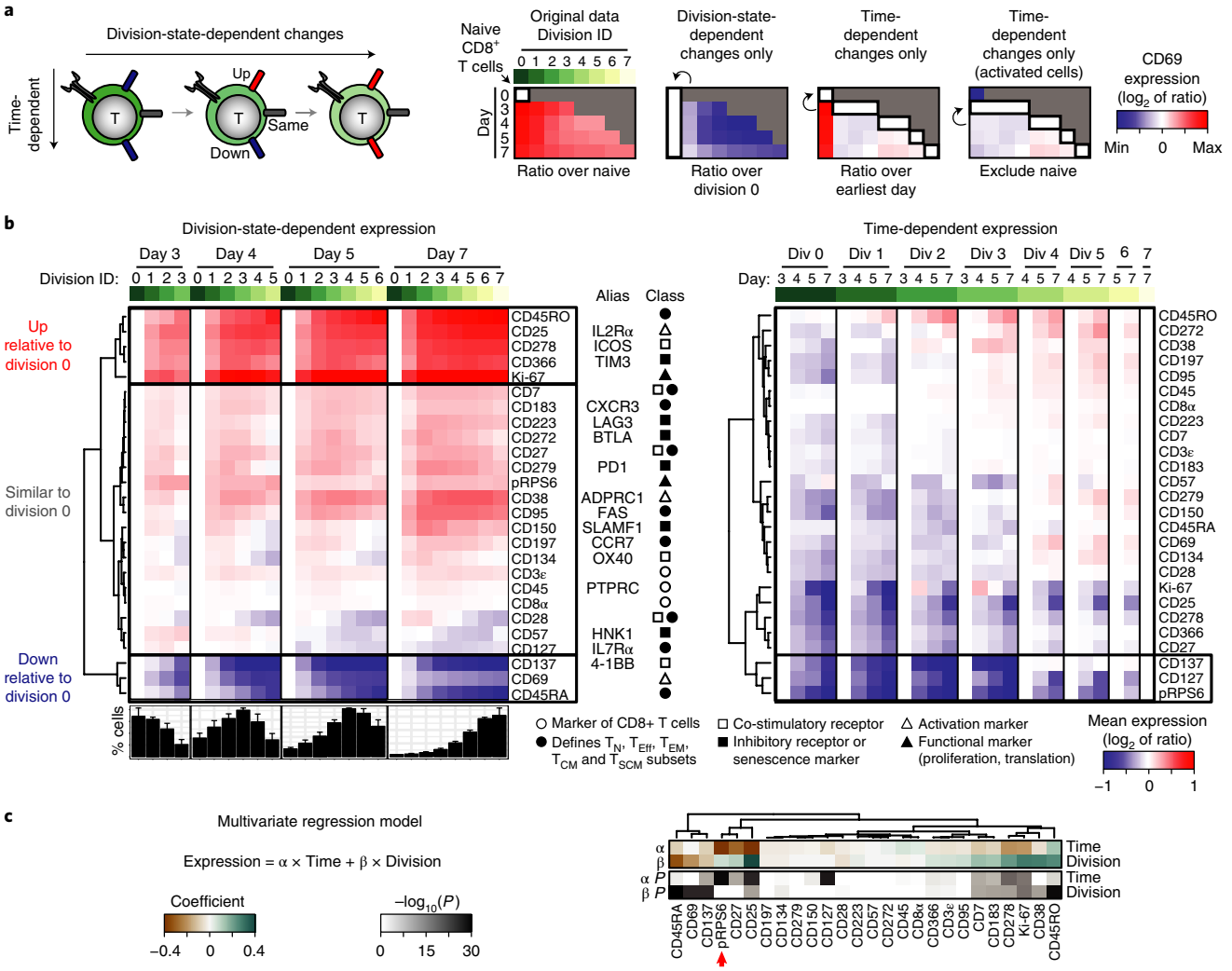

Fig. 2 | Uncoupling time and division state in expansion of naive CD8⁺ T cells shows that early differentiation is linked to both time and proliferation. **a**–**c**, Naive CFSE-labeled T cells were expanded using REP, collected on days 0,3,4,5 and 7 ($n = 26$ time-series samples from 6 cultures), analyzed by mass cytometry using the antibody panel in Supplementary Data 2, and gated on live non-apoptotic CFSE⁺ CD8⁺ T cells. **a**, A normalization scheme to examine time- and division-state-dependent changes as orthogonal dimensions. To focus on division-state-dependent changes only, expression is divided by division 0 at the same time point. To focus on time-dependent changes only, expression is divided by the earliest time point with the same division ID (except day 0, to focus on activated cells). CD69 is shown as an example. **b**, Changes in average division-state-dependent expression (left) or time-dependent expression (right) of 23 markers (plus CD3ε, CD8α and CD45, which were also used for gating) in CFSE-traced CD8⁺ T cells. See Supplementary Data 6 for additional information on each marker. Bar graphs show division state distribution on each day as mean ± s.e.m. **c**, A multivariate linear regression model to assess relative effects of time and division state on protein expression. Model coefficients and their *P*-values are shown as a heat map for each marker. Results in **a**–**c** are from 1 experiment representative of 3 experiments. T_N, naive T cells; T_{CM}, central memory T cells; T_{EM}, effector memory T cells; T_{SCM}, stem cell memory T cells.

expressing the CD57 senescence marker[11]. Since T_{SCM} cells are similar to naive T cells in their protein expression[12], allowing connections only among cells in consecutive division states ensured that the true division history defined cell locations in the final force-directed map. This map allowed us to devise a simple fluorescence-activated cell sorting (FACS) scheme to prospectively isolate and test functional properties of T_{SCM}-like and dysfunctional-phenotype subsets (Fig. 4a, right, and Supplementary Fig. 16). Upon re-stimulation, T_{SCM}-like cells had greater proliferative potential, greater resistance to apoptosis and less dysfunctional marker expression. Using intracellular staining, we confirmed that T_{SCM}-like cells produced more interleukin (IL)-2 and less interferon (IFN)-γ and tumor necrosis factor (TNF)-α (Supplementary Fig. 17), as expected for T_{SCM}-enriched cells[21].

DPT analysis confirmed the minimally differentiated state of T_{SCM}-like cells as DPT^{low} (Fig. 4b and Supplementary Fig. 13). Notably, DPT correlated with pRPS6, which is indicative of mTOR pathway activity (Fig. 4a,b, Supplementary Figs. 13–15 and Supplementary Data 7). The DPT–pRPS6 correlation remained irrespective of division state (Supplementary Fig. 18, black box), but pRPS6 decreased the most with time (Fig. 3c). These findings, together with high undivided cell diversity, led us to hypothesize that blocking signaling upstream of pRPS6 before the first division would direct naive T-cell differentiation toward the minimally differentiated (DPT^{low}) T_{SCM}-like fate (Fig. 4a). To test this, we selected an inhibitor of the mTOR pathway, rapamycin, and an inhibitor of the upstream TCR signaling pathway, ibrutinib (a dual BTK (Bruton's tyrosine kinase)

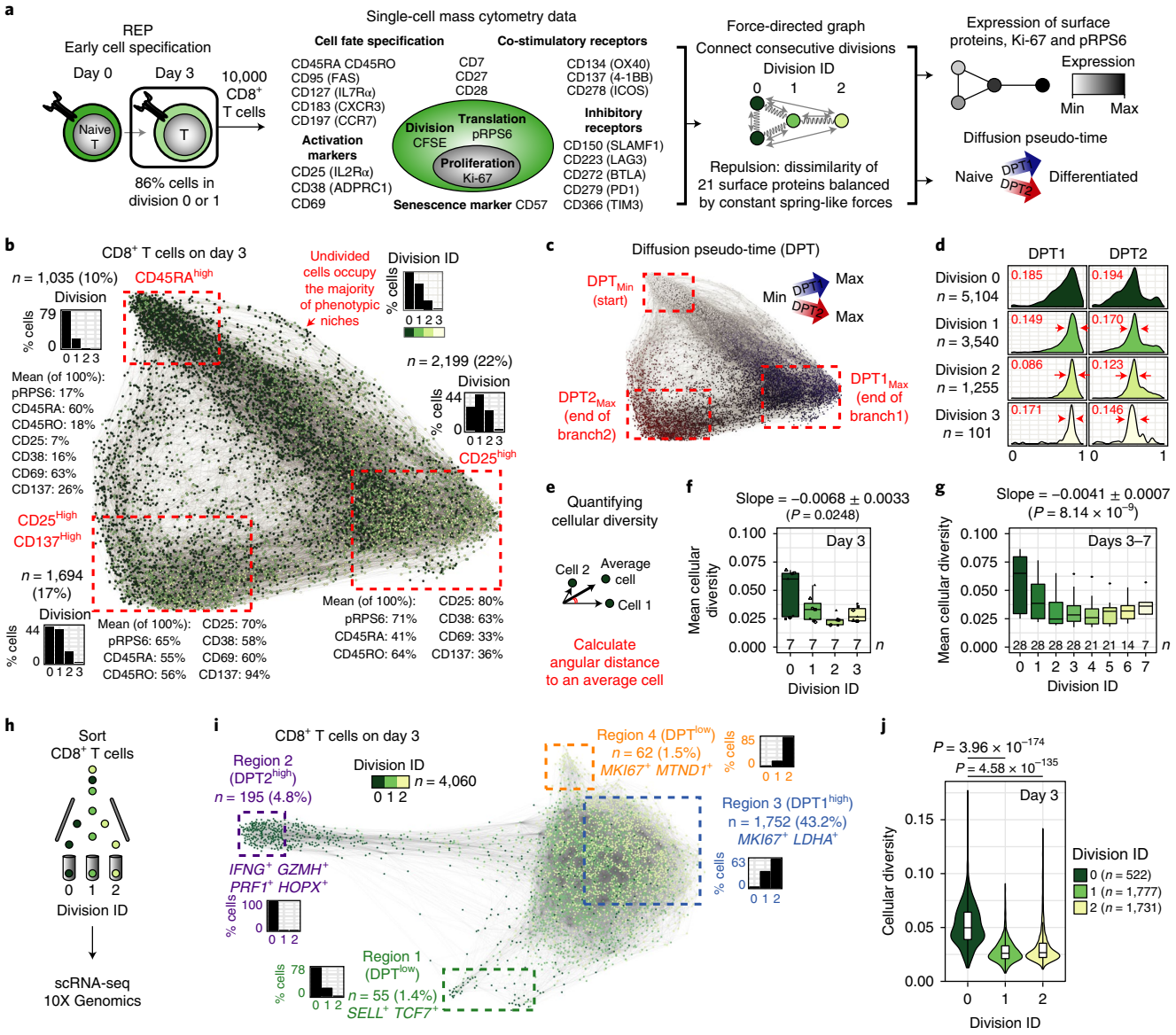

Fig. 3 | Undivided cells display the highest phenotypic diversity in early naive T-cell differentiation. a, Force-directed graph constructed with 10,000 CFSE$^+$ CD8$^+$ T cells from day 3 of REP, analyzed by mass cytometry using the antibody panel in Supplementary Data 2. Cells repel on the basis of expression of 21 surface proteins. Edges connect only cells in neighboring division states. **b**, Division IDs overlaid onto phenotypic map from **a**. Marker expression was scaled to 0–100% before calculating mean expression within each region. **c**, DPT calculated using 21 surface proteins and overlaid onto the graph from **b**. Colors were scaled to emphasize separation of DPT1 and DPT2. **d**, DPT histograms separated by division. Red arrows indicate the narrowing in DPT s.d. within each division. Results in **b**–**d** are from 1 donor representative of 5 donors. **e**, High-dimensional phenotypic diversity, estimated as a cosine distance to an average cell within each division state. **f**, Mean phenotypic diversity of CFSE$^+$ CD8$^+$ T cells on day 3 ($n = 7$ REP cultures). **g**, Mean phenotypic diversity on days 3, 4, 5 and 7 ($n = 28$ time-series samples from $n = 7$ REP cultures). Phenotypic diversity in **f**,**g** was calculated as described in **e** using 18 common proteins. Box plots show quartiles with a band at median, whiskers indicating 1.5 IQR, and outliers shown separately. To assess evidence for a decrease in phenotypic diversity with division, we used linear mixed-effects models; slope ± s.e.m. and *P*-values are shown above each plot. **h**–**j**, 10,000 CFSE$^+$ CD8$^+$ T cells from divisions 0, 1 and 2 were sorted for droplet-based single-cell RNA-seq on day 3 of REP. Out of 19,222 genes detected in $n = 4,060$ cells (division 0: $n = 522$; division 1: $n = 1,777$; division 2: $n = 1,731$ sequenced in 1 experiment), we selected the 1,000 most variably expressed genes for analysis in **i**,**j**. **h**, Experimental outline. **i**, A force-directed graph constructed as in **a**. **j**, Phenotypic diversity calculated as in **e**. Violin plots show a kernel density estimate with a box plot, which contains quartiles with a band at median and whiskers indicating 1.5 IQR. Kruskal–Wallis *H* test (one-way ANOVA on ranks): $P = 1.58 \times 10^{-177}$; two-sided Wilcoxon Mann–Whitney (WMW) *U* test comparing division 0 versus division 1, $P = 3.96 \times 10^{-174}$; comparing division 0 versus division 2, $P = 4.58 \times 10^{-135}$. WMW *P*-values were corrected for multiple hypotheses testing using Bonferroni correction.

and ITK (IL-2-inducible T-cell kinase) inhibitor that inhibits ITK downstream of the TCR[22]) and administered them at higher concentrations during the initial activation (days 0–2) than during the high proliferative phase (days 3–7). We found that ibrutinib skewed T-cell differentiation away from the pRPS6^{high} path and toward the pRPS6^{low} path ending at the T_{SCM}-like state (Fig. 4b,c, Supplementary Figs. 15 and 19, and Supplementary Data 8). At the concentration tested, rapamycin reduced overall

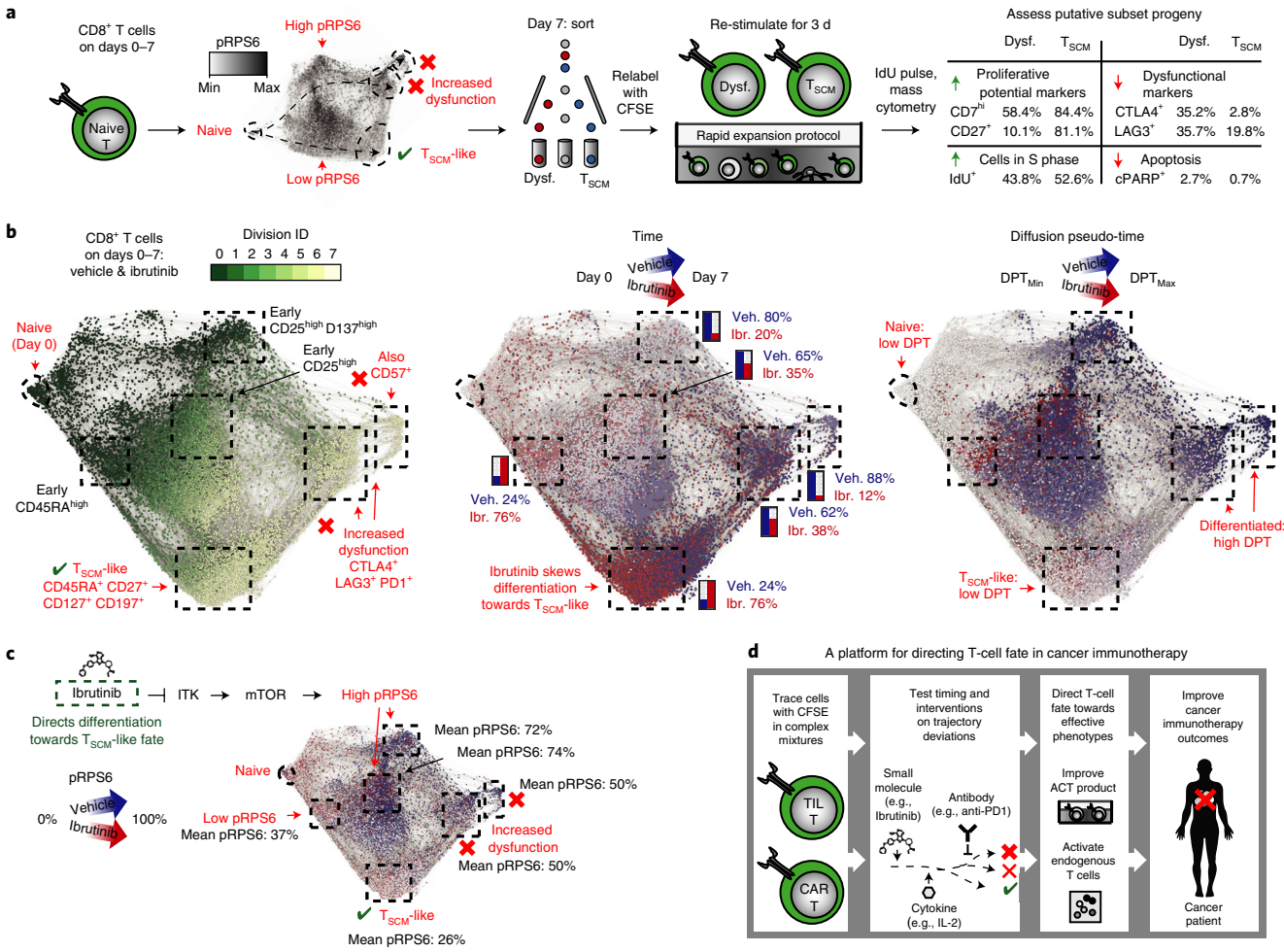

Fig. 4 | Ibrutinib directs naive T-cell differentiation toward T_{SCM}-like state. a, Naive CFSE$^+$ CD8$^+$ T-cell differentiation in REP converges onto T_{SCM}-like cells (pRPS6^{low} path) and cells with a dysfunctional (dysf.) phenotype (pRPS6^{high} path) by day 7 (Supplementary Figs. 13 and 14), with properties assessed in re-stimulation experiments (Supplementary Fig. 16) and summarized at right. **b**, REP cultures were treated with either vehicle (DMSO; Veh.) or ibrutinib (Ibr.), collected on days 0,3,4,5 and 7, and assessed by mass cytometry using the antibody panel in Supplementary Data 3. CFSE$^+$ CD8$^+$ T cells were pooled into a force-directed graph constructed using 27 surface proteins, with edges connecting only cells in neighboring divisions. Naive T-cell differentiation can be observed across divisions (left), time (center) or DPT (right) when these are overlaid on the graph. DPT was calculated using 27 surface proteins (separately for each treatment condition) and then scaled from 0 to 1 to improve visibility (DPT values for ibrutinib appear inflated on average 2.2-fold). Graph regions were defined using individual marker expression (Supplementary Fig. 15). Results were nearly identical when only proteins from the original panel (Supplementary Data 2) were used instead of the extended panel (Supplementary Data 3). **c**, pRPS6 overlaid onto the graph from **b** and colored by treatment condition. A signaling pathway links ibrutinib to pRPS6. Results in **b**,**c** are from 1 donor representative of 3 donors from 2 experiments. **d**, A summary of potential cancer immunotherapy applications of the platform presented here. Tracing fate of CFSE$^+$ tumor-infiltrating lymphocytes (TILs) or CAR T cells across time and divisions in complex cell mixtures may be useful for rationally selecting timing and interventions for guiding T-cell fate during ex vivo expansion for ACT. These insights may be later used for designing better drugs to improve T-cell function in situ.

proliferation and hindered differentiation by locking T cells in a naive-like CD127^{high} state (Supplementary Figs. 19 and 20 and Supplementary Data 8). Thus, early tuning of TCR or mTOR signaling had pronounced effects on phenotypic output.

Mechanistically, ibrutinib affected differentiation early in time and division. Namely, on day 3 all divisions had significantly lower DPT (division 0 $P = 2.57 \times 10^{-118}$, division 1 $P = 2.26 \times 10^{-65}$, Wilcoxon Mann–Whitney U test with Bonferroni correction for multiple hypothesis testing; Supplementary Fig. 19c) and were closer to the T_{SCM}-like state than vehicle-treated cells (Supplementary Fig. 21). Delaying ibrutinib treatment until day 3 reduced the fate skewing effect (Supplementary Fig. 22). Ibrutinib reduced apoptosis and cell death in both pRPS6$^+$ and pRPS6$^-$ compartments (Supplementary Data 8), arguing for redirection of naive-derived CD8$^+$ cells toward the T_{SCM}-like differentiation endpoint and against drug-induced subset selection.

T_{SCM} subset enrichment in chimeric antigen receptor (CAR)-engineered T cells enhances intracellular production of IL-2, but not of effector cytokines IFN-γ and TNF-α, when examined in bulk[21]. Similarly, ibrutinib enrichment of T_{SCM}-like subset improved intracellular production of IL-2, but not of IFN-γ and TNF-α, in bulk CD8$^+$ T cells (Supplementary Fig. 23). As expected[21], the benefit of T_{SCM} enrichment was the increased IFN-γ and TNF-α production by effector T cells generated in the presence of ibrutinib (Supplementary Fig. 24). Adding ibrutinib until day 3 only was sufficient to partially skew cells toward T_{SCM}-like fate and superior to both vehicle and continuous ibrutinib treatment in enhancing intracellular IL-2 and IFN-γ production by bulk CD8$^+$ T cells (Supplementary Figs. 23–25).

Uncoupling the sequence of cellular transitions through phenotypic space in the context of time and division states is essential for creating better models of cellular differentiation. Here we present a method for simultaneously tracing the proliferative history and phenotype of chemically labeled cells using highly multiplexed single-cell mass cytometry. While applied to primary human T cells here, we believe that this approach is generally applicable to tracing cell fate in complex mixtures for a variety of primary samples and cell lines[23], as well as to animal models of transplantation in which input material or genetic tracing could be limited.

We found early differentiation of naive CD8$^+$ T cells during expansion for immunotherapy to be linked to division state. Using a comprehensive panel of T-cell specialization and exhaustion markers, we established that undivided cells had the highest phenotypic diversity. Unbiased single-cell RNA-seq confirmed this observation and identified gene expression programs driving diversity. While we uncovered some mechanisms that linked division state and early cell fate choices, we did not investigate how cells acquired diverse phenotypes without division. Possibilities include the intrinsic predisposition of clonally derived naive T cells to produce diverse proportions of effector and memory populations[2,3], differences in TCR signaling, and co-receptor engagement[24,25]. Our results do not contradict asymmetric division, which influences T-cell fate[1,4].

The origin of T_{SCM} cells is of great interest[12]. While we did not trace fates of individual cells over time, our data suggest that, in the context of REP, T_{SCM}-like cells arise from a CD45RA^{high} subpopulation with low pRPS6 signaling. These cells are CD25^{low}, indicating that our data are consistent with observations that CD25^{high} CD8$^+$ T cells give rise to terminally differentiated and short-lived effector cells, whereas CD25^{low} cells eventually give rise to functional long-lived memory cells[26]. True T_{SCM} and dysfunctional states are more distant and not fully represented in REP[10], a model system that was not designed to mimic the normal T-cell differentiation processes. Further studies on the mechanisms linking proliferation to differentiation in vivo could benefit from this method.

We believe that our approach of identifying optimal intervention strategies on the basis of high-resolution maps of normal cellular differentiation will be broadly applicable to guiding the fate of endogenous or engineered T lymphocytes in cancer immunotherapy (Fig. 4d). Here, we selected ibrutinib to direct naive T-cell fate toward the T_{SCM}-like state. While ibrutinib reduced pRPS6 signaling and enhanced the expansion into our T_{SCM}-like cell compartment, we cannot rule out indirect effects of the inhibitor on antigen-presenting cells. In the future, ibrutinib could be useful for directing tumor-infiltrating T lymphocytes or CAR T cells toward T_{SCM} or other desired fates, which is an important direction in cancer immunotherapy research[12,21]. Our results may also help explain the recently observed T_{SCM} expansion in patients with chronic lymphocytic leukemia receiving ibrutinib[27], as well as the improvement in CAR T efficacy when administered after or with ibrutinib for treatment of this disease in the clinic[28–30].

This framework for tracing and directing the fate of labeled T cells should be broadly useful in stem cell biology and hematology and could improve clinical outcomes in cancer immunotherapy.

Online content

Any methods, additional references, Nature Research reporting summaries, source data, statements of data availability, and associated accession codes are available at https://doi.org/10.1038/s41587-019-0033-2.

Received: 31 October 2017; Accepted: 21 December 2018;
Published online: 11 February 2019

References

1. Chang, J. T. et al. Asymmetric T lymphocyte division in the initiation of adaptive immune responses. *Science* **315**, 1687–1691 (2007).
2. Gerlach, C. et al. Heterogeneous differentiation patterns of individual CD8$^+$ T cells. *Science* **340**, 635–639 (2013).
3. Tubo, N. J. et al. Most microbe-specific naïve CD4$^+$ T cells produce memory cells during infection. *Science* **351**, 511–514 (2016).
4. Reiner, S. L. & Adams, W. C. Lymphocyte fate specification as a deterministic but highly plastic process. *Nat. Rev. Immunol.* **14**, 699–704 (2014).
5. Woodworth, M. B., Girskis, K. M. & Walsh, C. A. Building a lineage from single cells: genetic techniques for cell lineage tracking. *Nat. Rev. Genet.* **18**, 230–244 (2017).
6. Quah, B. J. & Parish, C. R. New and improved methods for measuring lymphocyte proliferation in vitro and in vivo using CFSE-like fluorescent dyes. *J. Immunol. Methods* **379**, 1–14 (2012).
7. Bendall, S. C. et al. Single-cell mass cytometry of differential immune and drug responses across a human hematopoietic continuum. *Science* **332**, 687–696 (2011).
8. Lyons, A. B. & Parish, C. R. Determination of lymphocyte division by flow cytometry. *J. Immunol. Methods* **171**, 131–137 (1994).
9. Quah, B. J., Lyons, A. B. & Parish, C. R. The use of CFSE-like dyes for measuring lymphocyte proliferation: experimental considerations and biological variables. *Math. Model. Nat. Phenom.* **7**, 53–64 (2012).
10. Li, Y. & Kurlander, R. J. Comparison of anti-CD3 and anti-CD28-coated beads with soluble anti-CD3 for expanding human T cells: differing impact on CD8 T cell phenotype and responsiveness to restimulation. *J. Transl. Med.* **8**, 104 (2010).
11. Apetoh, L. et al. Consensus nomenclature for CD8$^+$ T cell phenotypes in cancer. *Oncoimmunology* **4**, e998538 (2015).
12. Gattinoni, L., Speiser, D. E., Lichterfeld, M. & Bonini, C. T memory stem cells in health and disease. *Nat. Med.* **23**, 18–27 (2017).
13. Rosenberg, S. A. & Restifo, N. P. Adoptive cell transfer as personalized immunotherapy for human cancer. *Science* **348**, 62–68 (2015).
14. Nish, S. A. et al. CD4+T cell effector commitment coupled to self-renewal by asymmetric cell divisions. *J. Exp. Med.* **214**, 39–47 (2017).
15. Jacomy, M., Venturini, T., Heymann, S. & Bastian, M. ForceAtlas2, a continuous graph layout algorithm for handy network visualization designed for the Gephi software. *PLoS One* **9**, e98679 (2014).
16. Samusik, N., Good, Z., Spitzer, M. H., Davis, K. L. & Nolan, G. P. Automated mapping of phenotype space with single-cell data. *Nat. Methods* **13**, 493–496 (2016).
17. Zunder, E. R., Lujan, E., Goltsev, Y., Wernig, M. & Nolan, G. P. A continuous molecular roadmap to iPSC reprogramming through progression analysis of single-cell mass cytometry. *Cell Stem Cell* **16**, 323–337 (2015).
18. Coifman, R. R. et al. Geometric diffusions as a tool for harmonic analysis and structure definition of data: diffusion maps. *Proc. Natl Acad. Sci. USA* **102**, 7426–7431 (2005).
19. Tibshirani, R. Regression shrinkage and selection via the lasso. *J. R. Stat. Soc. Series B Stat. Methodol.* **58**, 267–288 (1996).
20. Xu, L., Zhang, Y., Luo, G. & Li, Y. The roles of stem cell memory T cells in hematological malignancies. *J. Hematol. Oncol.* **8**, 113 (2015).
21. Sabatino, M. et al. Generation of clinical-grade CD19-specific CAR-modified CD8+memory stem cells for the treatment of human B-cell malignancies. *Blood* **128**, 519–528 (2016).
22. Dubovsky, J. A. et al. Ibrutinib is an irreversible molecular inhibitor of ITK driving a Th1-selective pressure in T lymphocytes. *Blood* **122**, 2539–2549 (2013).
23. Begum, J. et al. A method for evaluating the use of fluorescent dyes to track proliferation in cell lines by dye dilution. *Cytometry A* **83**, 1085–1095 (2013).
24. Marchingo, J. M. et al. Antigen affinity, costimulation, and cytokine inputs sum linearly to amplify T cell expansion. *Science* **346**, 1123–1127 (2014).
25. Salter, A. I. et al. Phosphoproteomic analysis of chimeric antigen receptor signaling reveals kinetic and quantitative differences that affect cell function. *Sci. Signal.* **11**, eaat6753 (2018).
26. Kalia, V. et al. Prolonged interleukin-2Rα expression on virus-specific CD8+T cells favors terminal-effector differentiation in vivo. *Immunity* **32**, 91–103 (2010).
27. Long, M. et al. Ibrutinib treatment improves T cell number and function in CLL patients. *J. Clin. Invest.* **127**, 3052–3064 (2017).
28. Turtle, C. J. et al. Durable molecular remissions in chronic lymphocytic leukemia treated with CD19-specific chimeric antigen receptor-modified T cells after failure of ibrutinib. *J. Clin. Oncol.* **35**, 3010–3020 (2017).
29. Fraietta, J. A. et al. Ibrutinib enhances chimeric antigen receptor T-cell engraftment and efficacy in leukemia. *Blood* **127**, 1117–1127 (2016).
30. Gill, S. et al. CD19 CAR-T cells combined with ibrutinib to induce complete remission in CLL. *J. Clin. Oncol.* **35**(Suppl), 7509 (2017).

Acknowledgements

We thank V. Gonzalez Munoz for panel design; J. Coller, D. Wagh (Stanford Functional Genomics Facility) and A. K. Shalek (UCSF) for single-cell RNA-seq advice; and S. Bhate, L. F. Yankielowicz-Keren, M. H. Spitzer, P. F. Gherardini and N. Agaheepour for insightful discussions. Z.G. was supported by the NIH training

grants 5T32AI007290-29, -30, -32, -33 and 2T32AI007290-31. G.P.N. was supported by NIH grants R01CA184968, 1R01GM10983601, 1R01NS08953301, 1R01CA19665701, R01HL120724, 1R21CA183660, R33CA0183692, 1R33CA183654-01, U19AI057229, 1U19AI100627, U54-UCA149145A, N01-HV-00242 HHSN26820100034C and 5UH2AR067676; NIH Northrop-Grumman Corporation subcontract 7500108142; FDA grant HHSF223201210194C; DOD grants OC110674 and W81XWH-14-1-0180; the NWCRA Entertainment Industry Foundation; and Bill and Melinda Gates Foundation grant OPP1113682. Z.G., G.P.N. and S.C.B. are members of the Parker Institute for Cancer Immunotherapy, which supported this work. S.C.B. was supported by a Damon Runyon Cancer Research Foundation Fellowship (DRG-2017-09); NIH 1DP2OD022550-01, 1R01AG056287-01, 1R01AG057915-01, 1-R00-GM104148-01, 1U24CA224309-01, 5U19AI116484-02 and U19 AI104209; and a Translational Research Award from the Stanford Cancer Institute. The Illumina HiSeq 4000 used here was purchased with NIH funds (award S10OD018220).

Author contributions

Z.G. and S.C.B. conceived the project and wrote the manuscript. Z.G. performed experiments and analyzed data. N.V.G. designed and carried out experiments on CFSE protocol optimization. L.B. designed and executed single-cell RNA-seq on prospectively isolated cell division states and assisted with initial antibody panel development. B.S. performed intracellular cytokine production assays and assisted with drug treatment experiments. N.S. implemented Vortex extensions. N.S. and R.T. advised on statistical and computational analyses. S.C.B. and G.P.N. secured funding and supervised the project. All authors read and commented on the manuscript.

Competing interests

Z.G., G.P.N. and S.C.B. are inventors on intellectual property applications for engineering T cells using methods described in this study.

Additional information

Supplementary information is available for this paper at https://doi.org/10.1038/s41587-019-0033-2.

Reprints and permissions information is available at www.nature.com/reprints.

Correspondence and requests for materials should be addressed to S.C.B.

Publisher's note: Springer Nature remains neutral with regard to jurisdictional claims in published maps and institutional affiliations.

Methods

Cells. Deidentified human blood was obtained from healthy adult donors under informed consent (Stanford Blood Center, Palo Alto, CA). Use of these samples was approved by Stanford's Institutional Review Board. Peripheral blood mononuclear cells (PBMCs) were isolated from Trima Accel leukocyte reduction system (LRS) chambers (Terumo BCT, Lakewood, CO) using Ficoll-Paque Plus (GE Healthcare, Chicago, IL, USA) density gradient centrifugation according to the manufacturer's instructions. For long-term storage, PBMCs were resuspended in FBS with 10% DMSO and stored in liquid nitrogen at a density of 1×10^7–5×10^7 cells/mL.

Cryopreserved PBMCs were thawed into cell culture medium (CCM; RPMI 1640 containing 10% FBS, 1× L-glutamine and 1× penicillin/streptomycin; Thermo Fisher Scientific Waltham, MA, USA) supplemented with 25 U/mL benzonase (Sigma-Aldrich, St. Louis, MO, USA). Cells were then pelleted for 5 min at 250 *g*, resuspended in 10 mL CCM, rested at 37 °C and 5% CO_2 for 60 min, filtered through a 40-µm strainer, and counted. Where indicated, naive T cells were enriched using a Naïve Pan T Cell Isolation Kit (Miltenyi Biotec #130-097-095, Bergisch Gladbach, Germany) according to manufacturer's instructions.

CFSE labeling. Unless otherwise noted, carboxyfluorescein succinimidyl ester (CFSE) labeling was performed as described by Quah and Parish[6,31]. Briefly, 50 µg carboxyfluorescein diacetate succinimidyl ester (CFDA-SE) was reconstituted in 18 µL DMSO (CellTrace CFSE Cell Proliferation Kit, Thermo Fisher Scientific #C34554) to create a 5 mM stock immediately before labeling. Cells were resuspended in 1 mL warm CCM and transferred into a new 15 mL Falcon tube lying horizontally. A drop containing 110 µL warm PBS was placed on a side of the tube, and 17.6 µL of 5 mM CFDA-SE was diluted into the drop. The tube was then quickly capped and turned upside right while being vortexed gently, yielding a final concentration of 80 µM CFDA-SE Cells were incubated for 5 min at room temperature, quenched by adding 9 mL warm CCM, and washed twice with 10 mL warm CCM. When only naive T cells were labeled with CFSE, they were combined with the CFSE-negative PBMC fraction devoid of naive T cells after labeling to restore original cell proportions. All centrifugation steps for live cells were done for 5 min at 250 *g*, room temperature. CFSE and labeled cells were protected from light throughout the experiment.

During protocol optimization, we tested the above labeling protocol for 0.1×10^7–10×10^7 cells and CFSE concentrations in range of 0.2 µM to 320 µM. We assessed long-term cell viability and proliferation. We also tested manufacturer's labeling protocol for CFSE concentrations of 0.2 µM to 20 µM, as well as another CFSE supplier (Biolegend #422701, San Diego, CA, USA).

Expansion and treatment of primary human T cells. T cells were induced to proliferate using the rapid expansion protocol (REP) for adoptive transfer therapies[10]. Briefly, ~4×10^7 cells were plated into a well of a 24-well plate with 2 mL CCM and 600 ng anti-CD3ε antibody (clone OKT3, Biolegend #317304). Where indicated, cells were pretreated with vehicle (DMSO), ibrutinib (PCI-32765; Cellagen Technology #C7327, San Diego, CA, USA; 700 ng/mL or 1.59 µM) or rapamycin (Cell Signaling Technology #9904 S, Danvers, MA, USA; 50 ng/mL or 54.70 nM) for 30 min. Starting at 48 h after activation, cells were maintained at ~2×10^6 cells/mL in CCM containing 300 ng/mL anti-CD3ε antibody and 50 U/mL (5 ng/mL) recombinant human IL-2 (PeproTech #200-02, Rocky Hill, NJ, USA) and relevant concentrations of chemical inhibitors (ibrutinib: 700 ng/mL or 1.59 µM on days 0–2, which was reduced to concentrations similar to those attained in vivo in mice[32,33] of 140 ng/mL or 318 nM on days 3–7; rapamycin: 50 ng/mL or 54.70 nM on days 0–2, which was reduced to concentrations similar to those attained in vivo in mice[34,35] of 10 ng/mL or 10.94 nM on days 3–7). Where indicated, ibrutinib was added only on either days 0–2 or days 3–7, with vehicle on the remaining days. In initial experiments, we tested a lower concentration of ibrutinib (140 ng/mL on days 0–7), whereupon the skewing effect was reduced (data not shown), and a higher concentration of ibrutinib (7 µg/mL on days 0–2, 1.4 µg/mL on days 3–7), whereupon we observed cell death and no proliferation (data not shown), before selecting the above ibrutinib treatment regimen. Samples containing 30% of cells from each condition were collected on days 0, 3, 4, 5 and 7, and then fixed and stored at –80 °C for flow cytometry and mass cytometry analyses.

Analysis of T_{SCM}-like and increased-dysfunction subsets. To compare the abilities of putative T_{SCM}-like and dysfunctional-phenotype cells to proliferate, persist and maintain a beneficial phenotype, naive $CFSE^+$ T cells were cultured using REP for 7 d to form these subsets. On the basis of the observed pattern of protein expression by day 7 (Supplementary Figs. 13 and 14), we defined a FACS staining panel and gating strategy (Supplementary Fig. 16b). Fc receptors were blocked using Human TruStain FcX (Biolegend #422302) following the manufacturer's instructions. Surface antibody staining was performed with anti-CD3ε–V500 (clone UCHT1, BD Biosciences #561416, Franklin Lakes, NJ, USA), anti-CD8α–PerCP (clone SK1, BD Biosciences #347314), anti-CD27–PE–Cy7 (clone O323, Biolegend #302837), anti-CD45RA–AlexaFluor700 (clone HI100, Biolegend #304119) and anti-CD279–PE (PD1; clone EH12.2H7, Biolegend #329905) antibodies for 30 min on ice in FACS buffer (PBS with 2% human serum and 2 mM EDTA). Cells were then washed once with FACS buffer and stained with 7-AAD (Biolegend #420404) to exclude dead cells following the manufacturer's instructions. Next, cells were resuspended in FACS buffer to sort out putative T_{SCM} and dysfunctional subsets on FACS Aria II (BD Biosciences). The post-sort purity of each subset was > 90%.

To assess the functional properties of the putative T_{SCM}-like and dysfunctional subsets, we relabeled the sorted cells with CFSE and cultured with new autologous CFSE-negative accessory cells using REP for 3 d (Supplementary Fig. 16a). To quantify the percentage of cells in S phase, the culture medium was supplemented with 100 µM 5-iodo-2′-deoxyuridine (IdU; Sigma-Aldrich #I7125-5G) 30 min before sample collection.

Intracellular cytokine production. To assess intracellular production of IL-2, IFN-γ and TNF-α at the indicated collection time points, cells were resuspended at 10^6 per mL and stimulated with 50 ng/mL phorbol 12-myristate 13-acetate (PMA; Sigma-Aldrich #P8139, dissolved in ethanol) and 500 ng/mL ionomycin (Sigma-Aldrich #I0634, dissolved in ethanol) in presence of 1× brefeldin A (Biolegend #420601) for 4 h. Cells were stained using the antibody panel in Supplementary Data 5 and assessed by mass cytometry.

Mass cytometry. Samples were processed as previously described[7]. To stain cells for viability, cisplatin[36] (Sigma-Aldrich #P4394) was reconstituted to 100 mM in DMSO and incubated at 37 °C for 3 d to prepare a stock solution, which was then stored in aliquots at –20 °C. Cell pellets were resuspended in 1 mL PBS containing 0.5 µM cisplatin, gently vortexed, incubated 5 min at room temperature, quenched with 3 mL CCM, pelleted, and resuspended in 1 mL CCM. Cells were fixed by adding 16% paraformaldehyde (PFA; Electron Microscopy Sciences, Hatfield, PA, USA) to a final concentration of 1.6%, gently vortexed, incubated 10 min at room temperature, and washed twice with cell staining media (CSM; PBS with 0.5% BSA, 0.02% sodium azide) to remove residual PFA. All centrifuging steps for fixed cells were done for 5 min at 600 *g*, 4 °C. Cell pellets were optionally stored at –80 °C.

With the exception of titrations, samples were palladium-barcoded and pooled as described[37] to improve staining consistency. Fc receptor blocking was performed with Human TruStain FcX (Biolegend #422302) following the manufacturer's instructions to prevent nonspecific antibody binding. Antibodies against surface antigens were pooled into a master mix in CSM yielding 50 µL (350 µL if barcoded) final reaction volumes per sample and filtered through a 0.1-µm filter (Millipore #UFC30VV00, Billerica, MA, USA) for 5 min at 1,000 *g* to remove antibody aggregates. Antibody master mix was then added to each sample, and cells were resuspended and incubated 30 min at room temperature. Mass cytometry antibody panels are listed in Supplementary Data 1–5. With the exception of antibodies purchased from Fluidigm (South San Francisco, CA, USA), all mass cytometry antibodies that were conjugated to reporter metal isotopes in-house were titrated to determine optimal staining concentrations before incorporating that antibody into a staining panel. Antibodies were conjugated using the MaxPar Antibody Conjugation Kit (Fluidigm) and titrated on cells both positive and negative for the target antigen expression to identify the concentration yielding the best signal-to-noise ratio. Following the surface staining, cells were washed with CSM, permeabilized with 4 °C methanol for 10 min on ice, washed twice with CSM, stained with an antibody master mix (prepared as above) against intracellular antigens in 50 µL (350 µL if barcoded) CSM for 30 min at room temperature, and washed once with CSM. To stain DNA, cells were incubated in PBS containing 1:5,000 $^{191}Ir/^{193}Ir$ MaxPar Nucleic Acid Intercalator (Fluidigm) and 1.6% PFA for 1–3 d at 4 °C. Just before analysis, cells were washed once with CSM and twice with filtered double-distilled water, resuspended in normalization beads[38] (EQ Beads, Fluidigm), filtered, and placed on ice. During event acquisition, cells were kept on ice and introduced into the CyTOF 2 (Fluidigm) using Super Sampler (Victorian Airship and Scientific Apparatus, Alamo, CA, USA). In addition to reporter metal isotopes listed in antibody panels (Supplementary Data 1–5), we recorded event length and channels ^{102}Pd, ^{104}Pd, ^{105}Pd, ^{106}Pd, ^{108}Pd and ^{110}Pd (barcoding); ^{140}Ce, ^{151}Eu, ^{153}Eu, ^{165}Ho and ^{175}Lu (bead normalization); ^{191}Ir and ^{193}Ir (DNA); ^{195}Pt and ^{196}Pt (dead cells); and ^{138}Ba (to help define single cells). In experiments quantifying IdU incorporation, we also recorded ^{127}I.

In optimization experiments for CFSE detection, we also tested alternative permeabilization methods (no permeabilization, 0.2% saponin, CFSE staining after permeabilization); multiple anti-FITC antibody clones, concentrations and detection channels (clone FIT-22 conjugated to ^{172}Yb, 0.25–16 µg/mL, Biolegend #408302; preconjugated clone FIT-22 on ^{144}Nd, 0.5–8 tests, Fluidigm #3144006B; clone F4/1 conjugated to ^{172}Yb, 0.25–16 µg/mL, Abcam #ab112511, Cambridge, UK; polyclonal antibody conjugated to ^{172}Yb, 1–64 µg/mL, Southern Biotech #6400-01, Birmingham, AL); and extended anti-FITC incubation time (60 instead of 30 min) for all clones.

Singe-cell RNA-sequencing of T-cell division states. Cells were collected as described on day 3 of REP. The lot of PBMCs was previously analyzed to obtain the exact timing to observe all three division states in the same culture. Here, ~10,000 live $CFSE^+$ $CD8^+$ T cells were prospectively isolated from division 0, 1 or 2 and resuspended in 100 µL CCM. Cells were stored on ice and processed the same day on the Chromium platform (10X Genomics, Pleasanton, CA, USA) at the Stanford Functional Genomics Facility for droplet-based 3′ single-cell RNA-sequencing per the manufacturer's instructions, with a target of 3,000 cells per sample and a sequencing depth of > 50,000 reads per cell. The sample libraries

were combined and run on a single lane of the HiSeq 4000 platform (Illumina, San Diego, CA, USA).

Flow cytometry. When comparing mass cytometry and flow cytometry data, viability staining was also performed with Fixable Violet Dead Cell Stain (Thermo Fisher Scientific #L34955). Samples were then fixed as described above and separated into two parts for both flow and mass cytometry analysis just before storage at −80 °C. Surface staining was performed with anti-CD3ε–APC (clone UCHT1, Biolegend #300412) and anti-CD8α–APC–H7 (clone SK1, BD Biosciences #560273) antibodies. Cells were then resuspended in 250 µL CSM and analyzed on LSRII flow cytometer (BD Biosciences).

Data processing. Mass cytometry data were normalized[38] and debarcoded[37]. Data were transformed using inverse hyperbolic sine (arcsinh) with a cofactor of 5 for DNA or protein expression[7] or a cofactor of 20 for CFSE. Single cells were gated using Cytobank software (http://www.cytobank.org) on the basis of event length and ^{191}Ir/^{193}Ir (DNA) content as described by Bendall et al.[7] Live non-apoptotic cells were gated based on ^{195}Pt content (viability)[36] and cleaved PARP. Hematopoietic cells were selected on the basis of CD45 expression. In initial experiments (antibody panel from Supplementary Data 1), CD45$^+$ cells were further gated to select CD8$^+$ T cells (CD3ε$^+$ CD4$^-$ CD8α$^+$ CD14$^-$ CD19$^-$ CD20$^-$), myeloid dendritic cells (CD3ε$^-$ CD11c$^+$ CD14$^-$ CD19$^-$ CD20$^-$ HLA-DR$^+$) or monocytes (CD3ε$^-$ CD14$^+$ CD19$^-$ CD20$^-$). In experiments focused on differentiation of CD8$^+$ T cells (antibody panels from Supplementary Data 2–5), we also excluded events that were CD33$^+$ (myeloid), CD61$^+$ (platelets), CD235$^+$ (erythrocytes) or TCRγδ$^+$ (γδ T cells). Where indicated, CFSE$^+$ cells were selected on the basis of a CFSE$^-$ control from the same day. An example gating strategy is provided in Supplementary Fig. 3a,b.

Flow cytometry data were transformed using arcsinh with a cofactor of 150. CD8$^+$ T cells were gated as single live CD3ε$^+$ CD8α$^+$ events.

Single-cell RNA-sequencing reads were aligned to the Genome Reference Consortium Human Build 38 (GRCh38), normalized for batch effects, and filtered for cell events using the Cell Ranger software (10X Genomics). A total of 4,060 cells were sequenced to an average of 52,040 post-normalization reads per cell capturing a median of 18,770 unique molecular identifier (UMI) counts per cell mapping to 3,544 unique genes per cell. The cell–gene matrix was further processed using the Cell Ranger R Kit software (10X Genomics) as described by Zheng et al.[39]. Briefly, we first selected genes with at least 1 UMI count in any given cell (19,222 genes). UMI counts were then normalized to UMI sums for each cell and multiplied by a median UMI count across cells. Next, the data were transformed by taking the natural logarithm of the resulting data matrix. Where indicated, we selected the 1,000 most variably expressed genes on the basis of normalized dispersion[39].

Division ID assignment. Single-cell data for CFSE$^+$ CD8$^+$ T cells were processed using R (http://www.r-project.org) and Bioconductor (http://www.bioconductor.org) software. To assign division IDs to cells in a given sample, we identified division peaks in $\log_2$-transformed CFSE ion count or fluorescence data using local regression. Centroid of division 0 peak and peak s.d. were estimated on the basis of those of nonproliferating control cells collected at the same time. Remaining division IDs were assigned to all cells where assignment confidence was ≥80% based on normal distribution modeling (or division −1 if not assigned). Top and bottom CFSE intensity cutoffs were set at 2 s.d. above division 0 and 2 s.d. below the maximum division, respectively. A modified FCS file with a "Division" column appended to original data was then exported for downstream analysis. Figure 1e shows a summary of the division ID assignment process.

Force-directed layout. To create force-directed graphs, we used Vortex software[16], which implements the ForceAtlas2 engine[15,16]. Here, we extended Vortex to only allow edge connections either between subsequent time points (as in the FLOW-MAP algorithm[17]) or between subsequent divisions. Data were sampled as indicated before graph construction. Cell dissimilarity, a basis for repulsive forces, was calculated on the basis of angular (cosine) distance in the indicated dimensions. Edges, a basis for spring-like attractive forces, connected each cell in the original high-dimensional space to its ten nearest neighbors, which also had to be within consecutive (−1, 0, +1) division states. See Fig. 3a for a summary of this process.

Diffusion maps. Diffusion maps embed single-cell data into diffusion components through a nonlinear transformation[18,40]. To perform the embedding, a matrix of diffusion distances is computed among all cells using the mathematics of heat diffusion and random-walk Markov chains. This matrix is then applied to calculate DPT, a metric based on the transition probability of a diffusion process. To embed data into diffusion components and to calculate DPT, we applied the Destiny[40] implementation of diffusion maps in R, which enables identification of up to two endpoints of a differentiation process. Diffusion maps were constructed using the angular distance metric and the same markers as in force-directed graphs. Diffusion components, DPT values, division IDs and time (days) were appended to the data, enabling visualization of these parameters in force-directed graphs using Vortex. Where indicated, DPT values for different treatment conditions were normalized to the 0–1 range for visualization purposes.

Statistical analysis. Statistical analysis was performed using R statistical software (http://www.r-project.org). To assess CFSE correlation between identical samples analyzed by flow and mass cytometry, we calculated Spearman's rank correlation coefficient using $\log_{10}$-transformed medians for each division ID or using the percentage of cells assigned the same division ID. When no comparison to flow cytometry was made, we calculated Spearman's rank correlation coefficient using arcsinh-transformed mass cytometry data. In each case, *P*-values were calculated using the correlation test. We tested normality assumption using the Shapiro–Wilk test. As the normality assumption was not met in statistical tests on single-cell data performed here, we applied the unpaired two-tailed Wilcoxon Mann–Whitney *U* test to assess statistical significance between two groups. When more than two groups were compared, we first used the Kruskal–Wallis *H* test (one-way analysis of variance on ranks) to check whether there were differences among treatment groups, followed by an unpaired two-tailed Wilcoxon Mann–Whitney test applied to each treatment pair and by Bonferroni correction for multiple hypothesis testing. To assess evidence for a decrease in mean phenotypic diversity with division across experiments, we used the lme4[41] implementation of linear mixed-effects models in R.

We used lasso[19,42,43] to identify markers associated with DPT. We allocated 80% of cells into a training set and 20% of cells into a test set using random sampling. To construct a lasso model, we used the glmnet[42] implementation of lasso in R, including a built-in cross-validation function to tune the L_1 regularization parameter λ. We then used all training data to construct the final model and applied that model to the test data to assess performance.

Reporting Summary. Further information on research design is available in the Nature Research Reporting Summary linked to this article.

Code availability

An extended version of the Java-based Vortex software[16] and documentation can be accessed at https://github.com/nolanlab/vortex.

Data availability

Single-cell data can be accessed at the Stanford Digital Repository (https://purl.stanford.edu/db057gb5997). Singe-cell RNA-sequencing data are also available on Gene Expression Omnibus (GEO accession code GSE119139).

References

31. Quah, B.J. & Parish, C.R. The use of carboxyfluorescein diacetate succinimidyl ester (CFSE) to monitor lymphocyte proliferation. *J. Vis. Exp.* https://doi.org/10.3791/2259 (2010).
32. Advani, R. H. et al. Bruton tyrosine kinase inhibitor ibrutinib (PCI-32765) has significant activity in patients with relapsed/refractory B-cell malignancies. *J. Clin. Oncol.* **31**, 88–94 (2013).
33. Marostica, E. et al. Population pharmacokinetic model of ibrutinib, a Bruton tyrosine kinase inhibitor, in patients with B cell malignancies. *Cancer Chemother. Pharmacol.* **75**, 111–121 (2015).
34. Araki, K. et al. mTOR regulates memory CD8 T-cell differentiation. *Nature* **460**, 108–112 (2009).
35. Stenton, S. B., Partovi, N. & Ensom, M. H. Sirolimus: the evidence for clinical pharmacokinetic monitoring. *Clin. Pharmacokinet.* **44**, 769–786 (2005).
36. Fienberg, H. G., Simonds, E. F., Fantl, W. J., Nolan, G. P. & Bodenmiller, B. A platinum-based covalent viability reagent for single-cell mass cytometry. *Cytometry A* **81**, 467–475 (2012).
37. Zunder, E. R. et al. Palladium-based mass tag cell barcoding with a doublet-filtering scheme and single-cell deconvolution algorithm. *Nat. Protoc.* **10**, 316–333 (2015).
38. Finck, R. et al. Normalization of mass cytometry data with bead standards. *Cytometry A* **83**, 483–494 (2013).
39. Zheng, G. X. et al. Massively parallel digital transcriptional profiling of single cells. *Nat. Commun.* **8**, 14049 (2017).
40. Angerer, P. et al. destiny: diffusion maps for large-scale single-cell data in R. *Bioinformatics* **32**, 1241–1243 (2016).
41. Bates, D., Machler, M., Bolker, B. M. & Walker, S. C. Fitting linear mixed-effects models using lme4. *J. Stat. Softw.* **67**, 1–48 (2015).
42. Friedman, J., Hastie, T. & Tibshirani, R. Regularization paths for generalized linear models via coordinate descent. *J. Stat. Softw.* **33**, 1–22 (2010).
43. James, G., Witten, D., Hastie, T. & Tibshirani, R. *An Introduction to Statistical Learning with Applications in R* 6th edn (Springer Texts in Statistics, New York, 2015).